Online-Parameter-Estimation-Based Control Strategy Combining MTPA and Flux-Weakening for Variable Flux Memory Machines

Yuxiang Zhong, Heyun Lin, *Senior Member, IEEE*, Zhiyong Chen, Shukang Lyu, *Student Member, IEEE*, and Hui Yang, *Member, IEEE*

***Abstract*—This article proposes a novel online-parameter-estimation-based control strategy for high efficiency and wide speed operation of variable flux memory machine (VFMM), which combines maximum-torque-per-ampere and flux-weakening (FW) technologies. The PM flux linkage is estimated from a newly developed linear active-disturbance-rejection-based feedforward decoupling (LADR-FFD) current controller, while the *dq*-axis inductances are estimated by employing the recursive least squares algorithm. In the proposed strategy, VFMM is controlled by using only two magnetization states (MSs), namely highest and lowest MSs, to avoid frequent MS manipulation. In the high-speed region of each MS, a continuous *d*-axis current is applied to stator windings to weaken the air-gap flux for further speed range extension by combining the feedforward and feedback FW approaches. The design procedure of the LADR-FFD current controller and the online estimation methods of the PM flux linkage and *dq*-axis inductances are first introduced. The proposed online-parameter-estimation-based control strategy is subsequently interpreted with the help of formulas and diagrams. The feasibility and effectiveness of the proposed control strategy are verified through experimental measurements on a hybrid magnetic circuit VFMM prototype.**

***Index Terms*—Flux-weakening (FW), linear active disturbance rejection, maximum-torque-per-ampere (MTPA) control, online PM flux linkage estimation, variable flux memory machines (VFMMs).**

I. Introduction

VARIABLE flux memory machine (VFMM) has been recognized as a wide-speed permanent magnet (PM) machine in the true sense, since its air-gap flux can be flexibly adjusted through changing the magnetization state (MS) of the equipped low coercive force (LCF) PM by applying a short *d*-axis current pulse [1]–[5]. Compared with traditional PM synchronous machines (PMSMs), VFMM has less excitation loss in flux-weakening (FW) region, improving the operation efficiencies within a wider speed range. For this type of machine, its MSs should be properly selected according to running conditions. In the constant torque (low-speed) region, high MS is desired to produce large torque for heavy load. In the constant power (high-speed) region, low MS is expected to extend the speed range.

Some researchers have investigated the control strategies for VFMMs in the past decade, mainly focusing on the MS manipulation. In [3], several types of MS manipulation current pulses are designed and discussed by analyzing transient MS manipulation process. In [4], an optimal MS selection method and a steady-state loss minimization method are combined to further improve the machine efficiency. A hysteresis MS manipulation method is proposed to reduce the frequency of MS change and loss in [5]. In addition to MS manipulation, the control methods at each MS should also be studied to improve the overall efficiency for VFMMs, which has been rarely investigated.

In the constant torque region of each MS, maximum-torque-per-ampere (MTPA) control [6]–[9] can be adopted to reduce copper loss by utilizing the reluctance torque for VFMMs with saliency. Many pieces of literature have investigated MTPA approaches for traditional interior PMSMs (IPMSMs), such as signal injection methods and parameter-based methods. For signal injection MTPA methods, the variations in machine behavior, such as speed variations [6] and torque variations [7] should be detected, which will inevitably degrade the dynamic performance of machines. For parameter-based MTPA methods, the variations of machine inductances make it difficult to maximize the torque output capability. Lookup table (LUT) [8] is often used to store the measured inductance values under the different *dq*-axis currents. However, more LUTs are required for VFMMs due to they can operate in many MSs. An artificial-neural-network-based (MTPA) control for VFMM is proposed in [10] to address the control difficulty caused by the nonlinear inductance properties and the variable-flux characteristics [11]. However, the ANN training process is very time consuming and will inevitably increase the computational burden of the processors.

Manuscript received May 18, 2021; revised August 24, 2021; accepted November 5, 2021. Date of publication November 9, 2021; date of current version December 31, 2021. This work was supported in part by the National Natural Science Foundation of China under Grants 52037002 and 52077033, in part by Key R&D Program of Jiangsu Province under Grant BE2021052, and in part by the "Thousand Talents Plan" Project of Jiangxi Province under Grant jxsq2020102088. Recommended for publication by Associate Editor H. Hofmann. *(Corresponding author: Heyun Lin.)*

The authors are with the School of Electrical Engineering, Suzhou Institute, Southeast University, Nanjing 210096, China (e-mail: seu_emat_zhongyx@163.com; hyling@seu.edu.cn; seu_emat_chenzy@163.com; seueelab_lsk@163.com; huiyang@seu.edu.cn).

Color versions of one or more figures in this article are available at https://doi.org/10.1109/TPEL.2021.3126581.

Digital Object Identifier 10.1109/TPEL.2021.3126581

In the constant power region, the speed range of VFMM can be expanded by reducing the PM flux linkage through decreasing the MS of LCF PMs. In order to further extend the speed range, FW control can be adopted by applying continuous *d*-axis currents at each MS. The FW control in the traditional PMSMs can be classified into the feedforward and feedback categories. In the feedforward FW control [12], [13], the parameter variations and the neglected winding resistance make it difficult to obtain the optimal FW current commands. While for the feedback FW control [14], the dynamic response of the current regulation is relatively poor. In addition to the above-mentioned problems, the FW control should also be combined well with the MS manipulation for VFMMs to extend the speed range while avoiding on-load demagnetization.

All the aforementioned problems in MTPA and FW controls are more prominent in VFMM due to its variable MSs. Online parameter estimation method is an alternative approach to address these problems. In [23], the online estimated parameters are used to achieve a torque compensation control scheme considering the wide variation of PM temperature by using the steepest descent method and the affine projection algorithm. In [24], an online parameter-based high-speed control is presented for IPMSMs, in which a novel adaptive backstepping-based nonlinear control technique is proposed to estimate machine parameters. The researches show that the online parameter estimation method can accurately acquire the *dq*-axis inductances and PM flux linkage online instead of using LUTs, which is more suitable for VFMMs.

This article proposes an online-parameter-estimation-based control strategy for high efficiency and wide speed operation of VFMM by combining the MTPA and FW controls. This article is organized as follows. In Section II, the topology and MS characteristics of the investigated hybrid magnetic circuit VFMM (HMC-VFMM) are introduced. In Section III, a linear active-disturbance-rejection-based feedforward decoupling (LADR-FFD) current controller is first established. Then, the estimation methods for the PM flux linkage and *dq*-axis inductances are elaborated. In Section IV, the proposed online-parameter-based control strategy for VFMMs is described in the form of a schematic diagram, and the controls of the new MTPA and FW under different MSs are interpreted in detail. The feasibility and effectiveness of the proposed control strategy are validated through experiments on an HMC-VFMM prototype in Section V. Finally, Section VI concludes this article.

II. Machine Topology and MS Characteristics

A. Machine Topology

Fig. 1 shows the topology of the investigated HMC-VFMM with a dual-layer high coercive force (HCF) PM configuration. The HMC structure combines the advantages of parallel and series magnetic circuits. The majority of HCF PM magnetic fluxes can be short-circuited within the rotor core by means of the parallel branch when the LCF PMs are demagnetized, thus the flux regulation range is increased. Moreover, the series magnetic circuit and the triangular *q*-axis barriers remarkably reduce the influences of the *q*-axis current on *d*-axis magnetic circuit, improving the on-load demagnetization withstand capability. The MS of the LCF PMs can be flexibly changed by applying a *d*-axis magnetizing current pulse. Thus, the speed range of the machine is extended with the regulation of the total PM flux linkage.

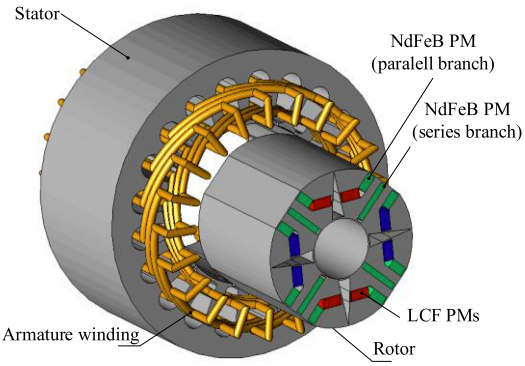

Fig. 1. Topology of investigated HMC-VFMM [2].

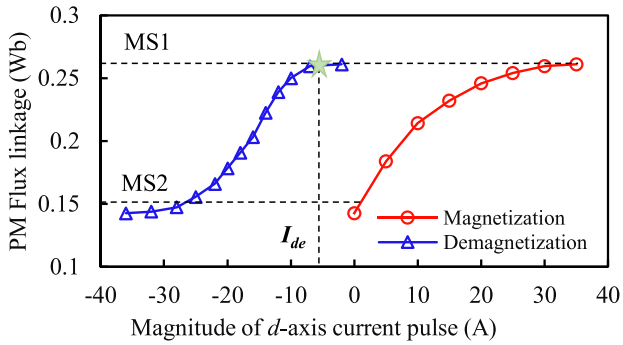

Fig. 2. Relationship between the PM flux linkage and the magnitude of the *d*-axis current pulse of the HMC-VFMM [2].

B. Characteristics of MSs

Fig. 2 presents the relationship between the PM flux linkage and the magnitude of *d*-axis current pulse of the HMC-VFMM. The PM flux linkage is calculated from the measured no-load back electromotive force (back EMF). The continuous flux adjustment method [15] is almost unpractical due to the frequent magnetization of the machine in engineering, which will produce pulsating torques accompanied by mechanical vibrations and noises. Therefore, only two specific MSs, MS1, and MS2, are selected to simplify the MS manipulation and maintain almost the same operation region compared with the continuous flux adjustment method. MS1 and MS2 are the highest and lowest MSs, of which the corresponding PM flux linkages ψ_{PM1} and ψ_{PM2} are 0.263 and 0.152 Wb, respectively. At MS1, the magnitude of the *d*-axis continuous current should be less than I_{de} (demagnetization current) to maintain the PM flux linkage and avoid unintended demagnetization, as shown in Fig. 2.

It is worth noting that the magnetization and demagnetization characteristics of the machine are relatively insensitive to temperature variations. The experimental results show that the

PM flux linkage has only a slight reduction (0.005 Wb, 1.9% of ψ_{PM1}) when the temperature rises from 22.4 to 65.2 °C.

III. Online Parameter Estimation for VFMM

A. Mathematical Model of VFMM

The voltage equation in the *d-q* reference frame and the electromagnetic torque T_e of VFMM can be expressed as

$$\begin{cases} u_d = Ri_d + L_d\frac{di_d}{dt} + \frac{d\psi_{PM}(i_d)}{dt} - \omega_e L_q i_q \\ u_q = Ri_q + L_q\frac{di_q}{dt} + \omega_e L_d i_d + \omega_e \psi_{PM}(i_d) \end{cases} \tag{1}$$

$$T_e = \frac{3}{2}p[\psi_{PM}(i_d)i_q + (L_d - L_q)i_d i_q] \tag{2}$$

where u_d and u_q are the *dq*-axis voltages, i_d and i_q are the *dq*-axis currents, R is the phase resistance, L_d and L_q are the *dq*-axis static inductances, considering saturation and cross-saturation effects [16], which are related to both i_d and i_q, ω_e is the rotor electrical angular speed, p is the number of pole pairs, and $\psi_{PM}(i_d)$ is the variable PM flux linkage, which is determined by the magnitude of *d*-axis current pulse. It should be noted that $d\psi_{PM}(i_d)/dt$ is approximately equal to zero under normal operations at a fixed MS, while $d\psi_{PM}(i_d)/dt$ cannot be neglected during MS manipulation, due to the drastic change of PM flux linkage.

B. LADR-FFD Current Controller Design

Based on the feedforward decoupling theory, the *dq*-axis feedforward voltage components, u_{d_ff} and u_{q_ff}, can be expressed as

$$\begin{cases} u_{d\_ff} = \hat{R}i_d - \omega_e \hat{L}_q i_q \\ u_{q\_ff} = \hat{R}i_q + \omega_e \hat{L}_d i_d \end{cases} \tag{3}$$

where superscript "^" denotes the estimation variables, and the initial values of $\hat{R}$, $\hat{L}_d$, and $\hat{L}_q$ are R_0, L_{d0}, and L_{q0}, respectively, which can be measured at no-load condition.

By substituting (3) into (1), the voltage equation can be rewritten as

$$\begin{cases} u_d = \underbrace{\hat{R}i_d - \omega_e \hat{L}_q i_q}_{u_{d\_ff}} + \hat{L}_d\frac{di_d}{dt} \\ \qquad + \underbrace{\Delta R i_d + \frac{d\psi_{PM}(i_d)}{dt} - \omega_e \Delta L_q i_q + \Delta L_d \frac{di_d}{dt}}_{u_{d\_dc}} \\ u_q = \underbrace{\hat{R}i_q + \omega_e \hat{L}_d i_d}_{u_{q\_ff}} + \hat{L}_q\frac{di_q}{dt} \\ \qquad + \underbrace{\Delta R i_q + \omega_e \Delta L_d i_d + \Delta L_q \frac{di_q}{dt} + \omega_e \psi_{PM}(i_d)}_{u_{q\_dc}} \end{cases} \tag{4}$$

where u_{d_dc} and u_{q_dc} are the *dq*-axis disturbance voltages, respectively, $\Delta R = R - \hat{R}$, $\Delta L_d = L_d - \hat{L}_d$, and $\Delta L_q = L_q - \hat{L}_q$.

By removing the feedforward voltage components, the voltage equation can be reformed as

$$\begin{cases} u_{d\_ladrc} = u_d - u_{d\_ff} = \hat{L}_d\frac{di_d}{dt} + u_{d\_dc} \\ u_{q\_ladrc} = u_q - u_{q\_ff} = \hat{L}_q\frac{di_q}{dt} + u_{q\_dc} \end{cases} \tag{5}$$

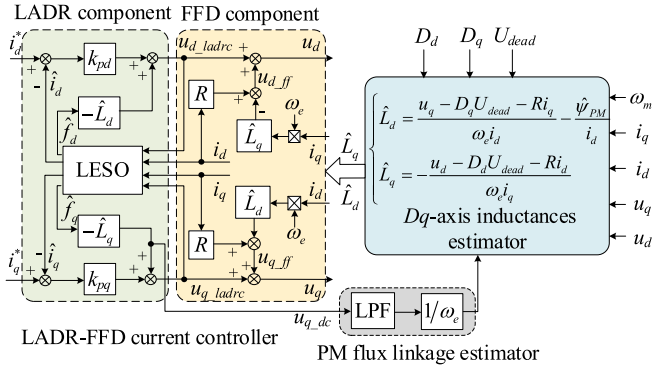

Fig. 3. Schematic diagram of the LADR-FFD current controller and online parameter estimators.

where u_{d_ladrc} and u_{q_ladrc} are the output values of the *dq*-axis LADR current controller. By selecting the state variables as

$$\mathbf{x}_1 = \mathbf{i} = \begin{bmatrix} i_d \\ i_q \end{bmatrix},\ \mathbf{x}_2 = \mathbf{f} = \begin{bmatrix} f_d \\ f_q \end{bmatrix} = \begin{bmatrix} -u_{d\_dc}\big/\hat{L}_d \\ -u_{q\_dc}\big/\hat{L}_q \end{bmatrix} \tag{6}$$

and assuming

$$\mathbf{u} = \mathbf{u}_{ladrc} = \begin{bmatrix} u_{d\_ladrc} \\ u_{q\_ladrc} \end{bmatrix},\ \mathbf{b} = \begin{bmatrix} 1\big/\hat{L}_d & 0 \\ 0 & 1\big/\hat{L}_q \end{bmatrix}. \tag{7}$$

Equation (6) can be further rewritten in the state equation as

$$\begin{cases} \dot{\hat{\mathbf{x}}}_1 = \hat{\mathbf{x}}_2 + b\mathbf{u} - \beta_1 \mathbf{e} \\ \dot{\hat{\mathbf{x}}}_2 = -\beta_2 \mathbf{e} \\ \mathbf{e} = \hat{\mathbf{x}}_1 - \mathbf{x}_1 \end{cases} \tag{8}$$

where f_d and f_q are the *dq*-axis disturbance components, $\beta_\mathbf{1}$ and $\beta_\mathbf{2}$ are the matrices of error feedback gains. A linear extended state observer (LESO) [25], [26] is constructed based on (8) to estimate the disturbance component. The structure of the LADR-FFD current controller is shown in Fig. 3.

C. Online Estimation of PM Flux Linkage and Error Analysis

In the proposed current controller, the PM flux linkage can be easily estimated through the *q*-axis disturbance voltage, u_{q_dc}, observed by the LESO, which can be expressed as

$$u_{q\_dc} = \Delta R i_q + \omega_e \Delta L_d i_d + \omega_e \psi_{PM}(i_d) + \Delta L_q \frac{di_q}{dt} \tag{9}$$

where $\Delta L_q di_q/dt$ is a periodic component at the steady-state, which can be eliminated by a low-pass filter. When the parameter variations of resistance and *d*-axis inductance are not obvious, $\omega_e \psi_{PM}(i_d)$ is the main part of u_{q_dc}, so that the estimated PM flux linkage at steady state can be calculated by

$$\hat{\psi}_{PM} = \frac{\mathrm{LPF}(u_{q\_dc})}{\omega_e}. \tag{10}$$

Based on (9) and (10), the estimation error of the PM flux linkage can be expressed as

$$\psi_{PM\_err} = \hat{\psi}_{PM} - \psi_{PM} = \frac{\Delta R i_q + \omega_e \Delta L_d i_d}{\omega_e}. \tag{11}$$

It can be found that ψ_{PM_err} is mainly caused by the variations of winding resistance and *d*-axis inductance. The machine temperature is the main cause of the resistance variation. The resistance variation of the studied machine is 0.08 Ω after 2-h full-load operation and ψ_{PM_err} caused by the resistance variation is only 0.003 Wb (1.1% of ψ_{PM1}) at rated speed 800 r/min, which can be neglected in this study. In the $i_d = 0$ control, ψ_{PM_err} is not affected by the *d*-axis inductance variation. However, its influence cannot be ignored in MTPA or FW control due to the existence of *d*-axis current, particularly at heavy load condition. Therefore, the *d*-axis inductances at different MS and load conditions should be accurately estimated to improve the estimation accuracy of the PM flux linkage.

D. Online Estimation of dq-Axis Inductances

In the process of estimating *dq*-axis inductances, the VSI nonlinearity, including the dead-time, turn-ON delay, turn-OFF delay, should be compensated. The offline compensation method [17]–[20] is adopted in this article due to its simplicity, and the distorted voltage U_{dead} can thus be written as

$$U_{dead}=\frac{T_{dead}+T_{on}-T_{off}}{T_s}U_{dc}+\frac{U_f+U_{diode}}{2} \tag{12}$$

where T_{dead} is the hardware deadtime, T_{on} and T_{off} are the turn-ON and turn-OFF delay times of the transistor, respectively, U_{dc} is the dc bus voltage, T_s is the sampling time of the processor, U_f and U_{diode} are the voltage drops of the transistor and freewheeling diode, respectively.

Consequently, the *dq*-axis voltage equation considering the VSI nonlinearity [17] can be obtained as

$$\begin{cases} u_d = u_d^* + D_d U_{dead} \\ u_q = u_q^* + D_q U_{dead} \end{cases} \tag{13}$$

where u_d^* and u_q^* are the real *dq*-axis voltages considering the VSI nonlinearity, U_{dead} is the magnitude of the distorted voltage in the *dq*-axis reference frame, D_d and D_q are the coefficients of the *dq*-axis distorted voltages, respectively, which can be expressed as follows:

$$\begin{bmatrix} D_d \\ D_q \end{bmatrix} = 2 \begin{bmatrix} \cos(\theta) & \cos(\theta-\frac{2\pi}{3}) & \cos(\theta+\frac{2\pi}{3}) \\ -\sin(\theta) & -\sin(\theta-\frac{2\pi}{3}) & \sin(\theta-\frac{\pi}{3}) \end{bmatrix} \times \begin{bmatrix} sign(i_a) \\ sign(i_b) \\ sign(i_c) \end{bmatrix} \tag{14}$$

where θ is the rotor position, *sign* is the symbolic function, and i_a, i_b, and i_c are the three-phase currents.

The derivative terms in the voltage equation can be neglected at steady state. Based on the simplified voltage equation and the estimated PM flux linkage $\hat{\psi}_{PM}$, the *dq*-axis inductances can be respectively estimated from

$$\begin{cases} \hat{L}_d = \frac{u_q - D_q U_{dead} - R i_q}{\omega_e i_d} - \frac{\hat{\psi}_{PM}}{i_d} \\ \hat{L}_q = -\frac{u_d - D_d U_{dead} - R i_d}{\omega_e i_q}. \end{cases} \tag{15}$$

The recursive least squares algorithm is employed for the *dq*-axis inductances estimation due to its good convergence and stability [21], [22]. The estimation object model is given as

$$Y(k) = \Theta^T Z(k) \tag{16}$$

where $Y(k)$ is the output vector, $\Theta(k)$ is the unknown parameter vector and $Z(k)$ is the signal vector. Then, the parameters can be estimated by using the following equations:

$$\hat{\Theta}(k) = \hat{\Theta}(k-1) + \frac{\mathbf{P}(k-1)Z(k)}{\lambda + Z^T(k)\mathbf{P}(k-1)Z(k)} \times \left(Y(k) - Z^T(k)\hat{\Theta}(k-1)\right) \tag{17}$$

$$\mathbf{P}(k) = \frac{1}{\lambda}\left(\mathbf{P}(k-1) - \frac{\mathbf{P}(k-1)Z(k)Z^T(k)\mathbf{P}(k-1)}{\lambda + Z^T(k)\mathbf{P}(k-1)Z(k)}\right) \tag{18}$$

where $\boldsymbol{P}(k)$ is the covariance vector and λ is the forgetting factor ($\lambda<1$). The *dq*-axis inductances can be estimated by expressing the model (15) in the form of (16).

As shown in Fig. 3, the estimated *dq*-axis inductances are updated to the LADR-FFD current controller to improve its robustness and control performance. When estimating L_d, the estimated PM flux linkage in the last sampling period will be used and updated into the L_d estimator. Similarly, when estimating PM flux linkage, the previous estimated L_d will also be utilized. Finally, the accurate PM flux linkage and *dq*-axis inductances can be simultaneously obtained by the self-tuning between the two estimators.

IV. Proposed Control Strategy for VFMM

The schematic diagram of the proposed online-parameter-estimation-based control strategy for high efficiency and wide speed operation of VFMM is illustrated in Fig. 4. It consists of two online parameter estimators, an MS controller and an MTPA&FW controller. The schematic diagram of the MS controller is shown in Fig. 5. First, the speed at the intersection of the torque-speed curves at the two MSs is set as switching speed (ω_1). When the speed ω_m is lower than ω_1, the machine should run at MS1, while when the speed ω_m exceeds ω_1, the machine should run at MS2. Then, a hysteresis controller [4] is utilized to reduce the frequency of MS manipulation, particularly when the machine is operating around ω_1. When receiving an MS manipulation command, the MS controller will be immediately activated to generate a transient current pulse to change the MS of LCF PMs. Besides, when the difference between the estimated and reference PM flux linkage is larger than the preset range due to unexpected PM working point drifting, the MS controller will apply a magnetizing or demagnetizing current pulse to recover the original MS.

The MTPA&FW controller makes the machine run in the MTPA or FW mode according to the speed and load conditions, generating corresponding *dq*-axis current commands. Fig. 6 shows the configuration of the controller at the two MSs, which incorporates the MTPA operation in the constant torque region and the FW operation in the constant power region, as well as the switch algorithm between them.

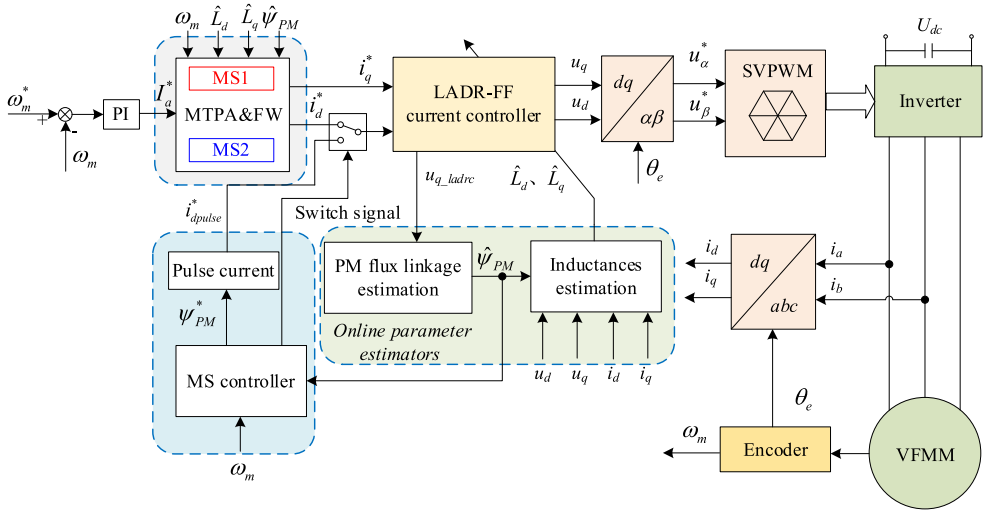

Fig. 4. Schematic diagram of the proposed online-parameter-estimation-based control strategy for VFMMs.

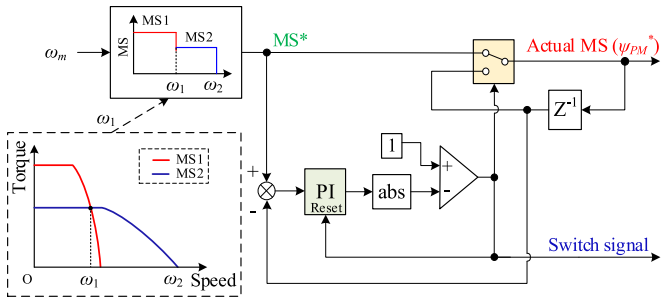

Fig. 5. Schematic diagram of the MS controller [4].

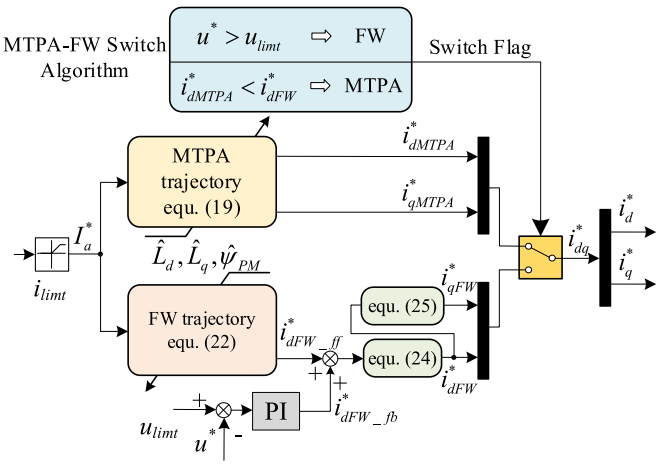

Fig. 6. Configuration of the MTPA&FW controller.

A. MTPA Control

In the constant torque region of each MS, the MTPA control is adopted to produce the maximum machine torque per ampere by utilizing the reluctance torque. Based on the torque (2) and the estimated machine parameters [22], the *dq*-axis currents under the MTPA control can be derived as

$$\begin{cases} i^*_{dMTPA} = \dfrac{\hat{\psi}_{PM}}{4(\hat{L}_q-\hat{L}_d)} - \sqrt{\dfrac{\hat{\psi}^2_{PM}}{16(\hat{L}_q-\hat{L}_d)^2} + \dfrac{I^{*2}_a}{2}} \\ i^*_{qMTPA} = \sqrt{I^{*2}_a - i^{*2}_{dMTPA}} \end{cases} \tag{19}$$

where I^*_a is the magnitude of current reference generated by the speed loop, as shown in Fig. 4. It should be noted that i^*_{dMTPA} should be limited to avoid unintended demagnetization at MS1 in theory. However, this limitation is unnecessary for the studied machine due to the relatively small difference between the *dq*-axis inductances.

Besides, the difference between the estimated *dq*-axis inductances should be first calculated to avoid the division by zero issue when solving (19). When the calculated difference is smaller than the preset range ε, the *dq*-axis currents under the MTPA control are taken as

$$if \left|\hat{L}_q - \hat{L}_d\right| \le \varepsilon, \begin{cases} i^*_{dMTPA} = 0 \\ i^*_{qMTPA} = I^*_a . \end{cases} \tag{20}$$

B. FW Control

Due to the limitation of inverter, the voltage and current of the machine should satisfy the following equations:

$$\begin{cases} u_d^2 + u_q^2 \le u_{limit}^2 \\ i_d^2 + i_q^2 \le i_{limit}^2 \end{cases} \tag{21}$$

where u_{limt} ($U_{dc}/\sqrt{3}$) and i_{limit} are the maximum amplitudes of phase voltage vector and current vector, respectively.

When the speed exceeds the rated speed of each MS, a continuous negative *d*-axis current should be increased to ensure the amplitude of voltage vector is within u_{limit}. In the steady-state operation, by substituting (1) into (21) and neglecting the voltage drop on the resistance, the *dq*-axis currents should satisfy

$$\begin{cases} \left(\hat{L}_q i_q\right)^2 + \left(\hat{L}_d i_d + \hat{\psi}_{PM}\right)^2 = \left(\frac{u_{limt}}{\omega_e}\right)^2 \\ i_d^2 + i_q^2 = I_a^{*2}. \end{cases} \tag{22}$$

A newly developed FW control combining feedforward and feedback approaches is proposed in this article to tradeoff between the fast response and robustness of current regulation [12]. The feedforward component of *d*-axis current under the FW control [23], $i^*_{\mathrm{dFW\_ff}}$, can be obtained as a tentative solution quickly by solving (22). The feedback component $i^*_{\mathrm{dFW\_fd}}$ is gained through the PI controller, in which the input and the feedback signals are u_{limt} and u^*, respectively, as shown in Fig. 6. Thus, the *d*-axis current under the FW control can be calculated as

$$i^*_{dFW}=i^*_{dFW\_ff}+i^*_{dFW\_fd}. \tag{23}$$

In the developed FW control, not only the fast response performance can be achieved by solving (22) but also the influence of neglecting resistance when solving (22) can be alleviated through the FW PI controller.

To avoid unintended demagnetization, the *d*-axis current of the machine at the two MSs should be constrained as

$$\begin{aligned}&\mathrm{MS1}, i^*_d=\begin{cases} i^*_d\ , i^*_d > I_{de} \\ I_{de}\ , i^*_d \le I_{de}\end{cases}\\ &\mathrm{MS2}, i^*_d=i^*_d.\end{aligned} \tag{24}$$

The *q*-axis current under the FW control can be expressed as

$$i^*_{qFW}=\sqrt{I^{*\,2}_a-i^{*2}_{dFW}}. \tag{25}$$

The switch algorithm between the MTPA and FW control modes is shown in Fig. 6. When u^* ($u^*=\sqrt{u_d^2+u_q^2}$) exceeds the voltage limitation u_{limit}, the machine will switch from the MTPA mode to the FW mode with a larger *d*-axis current. Then, if the magnitude of *d*-axis current in the MTPA mode i^*_{dMTPA} grows larger than that in the FW mode i^*_{dFW} , the machine will run in the MTPA mode. Therefore, the seamless transition between the MTPA and FW modes can be achieved by using the proposed switch algorithm.

In summary, the *dq*-axis reference currents are directly generated by solving (22) in the online-parameter- estimation-based MTPA control, in which the machine parameters are updated online, achieving fast transient response and good robust to parameter variation at any MS. On the other side, the newly developed FW control inherits the advantages of both the feedforward and feedback FW methods so that the fast response, stability, and robustness of current regulation can be guaranteed. Meanwhile, the on-load demagnetization of the studied machine can be avoided by restricting the magnitude of the *d*-axis continuous current.

V. Experimental Validation

Fig. 7 shows the experimental setup used for experimental validation of the proposed control strategy. The tested HMC-VFMM is connected with a torque meter and a servo motor, as shown in Fig. 7(a). The machine is fed by a three-phase half-bridge inverter consisting of six MOSFETs (FDA59N30). A STM32F407VET6 is used to implement the control strategy, and DACs (digital to analog conversion) are used to output variables to an oscilloscope. The main parameters of the prototype and

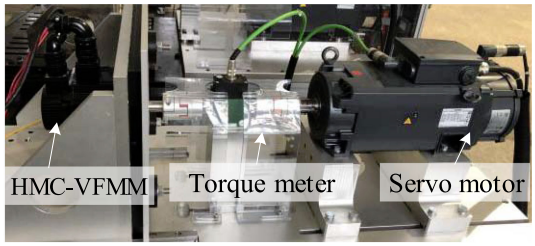

(a)

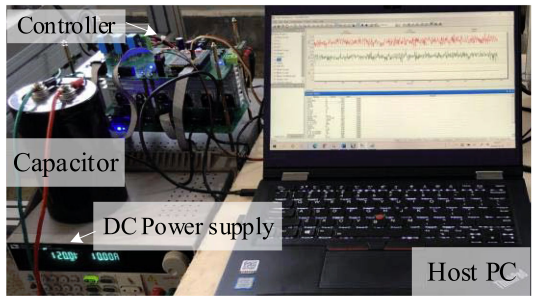

(b)

Fig. 7. Experimental setup. (a) Test rig of the HMC-VFMM prototype. (b) Control board.

TABLE I
Main Parameters of the HMC-VFMM Prototype, Definitions of Different MSs, and Experimental Setup Information [2]

Symbol	Quantity	Value
U_{dc}	DC bus voltage	100 V
P_N	rated power	500 W
n_N	rated speed	800 rpm
p	pole pairs	2
I_N	rated current	7.5 A
ψ_{PM1}	PM flux linkage at MS1	0.263 Wb
ψ_{PM2}	PM flux linkage at MS2	0.152 Wb
L_{d0}	nominal *d*-axis inductance	17 mH
L_{q0}	nominal *q*-axis inductance	32 mH
R	phase resistance	1.3 Ohm

TABLE II
Typical Electrical Parameters of VSI

Turn off delay T_{off}	0.715 µs
Turn on delay T_{on}	0.320 µs
Hardware dead time T_{dead}	2 µs
Sampling time T_s	100 µs
Voltage drop of the freewheeling diode U_{diode}	1.4 V
Static drain-source on-resistance of MOSFET R_{DS}	47 mΩ

the typical electrical parameters of VSI are tabulated in Tables I and II.

A. Performance of LADR-FFD Current Controller

Fig. 8 shows the current tracking performance during the MS manipulation by using the LADR-FFD current controller. The reference and real waveforms of a +35 A *d*-axis magnetizing current and a −25 A *d*-axis demagnetizing current are shown in Fig. 8(a) and (b), respectively. It can be found that the real current can track the reference value accurately.

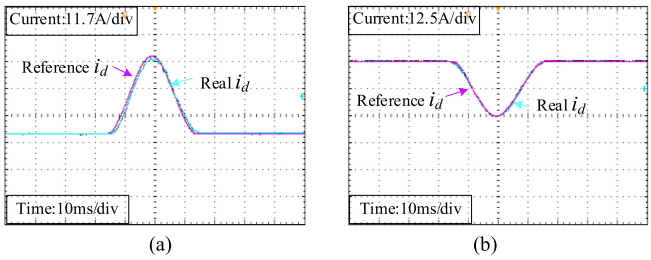

Fig. 8. Current tracking performance during MS manipulation. (a) $i_d = +35$ A. (b) $i_d = -25$ A.

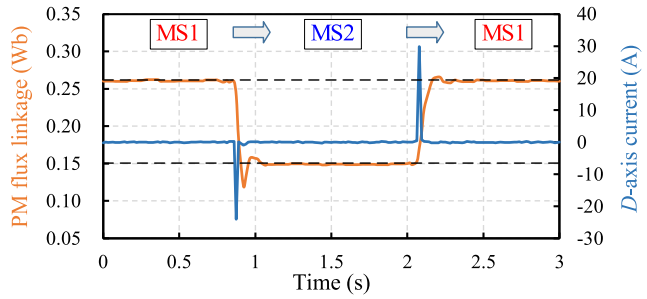

Fig. 9. Experimentally estimated PM flux linkages and d-axis current pulses at different MSs (600 r/min, rated load condition).

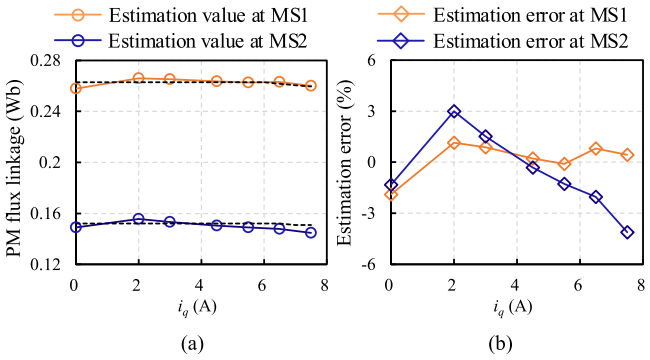

Fig. 10. PM flux linkage estimation results at MS1 (0.263 Wb, 600 r/min) and MS2 (0.152 Wb, 900 r/min), at different load conditions, under $i_d = 0$ control. (a) Estimation value. (b) Estimation error.

B. PM Flux Linkage Estimation

Fig. 9 illustrates the experimental waveforms of the estimated PM flux linkage and d-axis current pulse at different MSs. The machine is running at 600 r/min and rated load condition. It can be clearly observed that the estimation result by using the proposed method is very close to the real value at steady state and the estimation error can be accepted at both MS1 and MS2.

Fig. 10(a) and (b) shows the estimated PM flux linkage and the percent of estimation error against q-axis current when adopting the $i_d = 0$ control and the speeds are 600 r/min at MS1 and 900 r/min at MS2, respectively. In both the cases, the estimation results by using the proposed estimation method are close to the real values. The percent of maximum estimation error at the two MSs are within 4%. It should be noted that the inductance variation has no effect on the estimation results due to $i_d = 0$, according to (11).

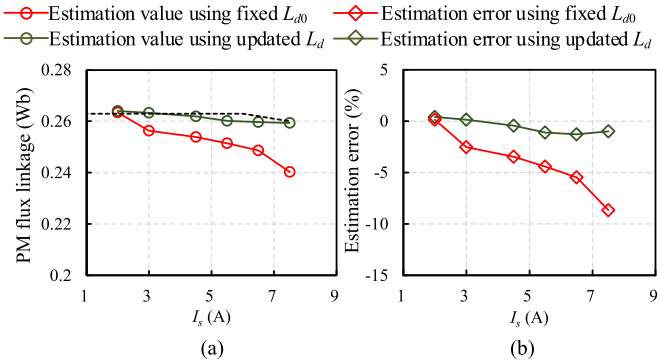

Fig. 11. Estimated PM flux linkages by using the fixed L_{d0} and online updated L_d at different load conditions under MTPA control, at MS1, 600 r/min. (a) Estimation value. (b) Estimation error.

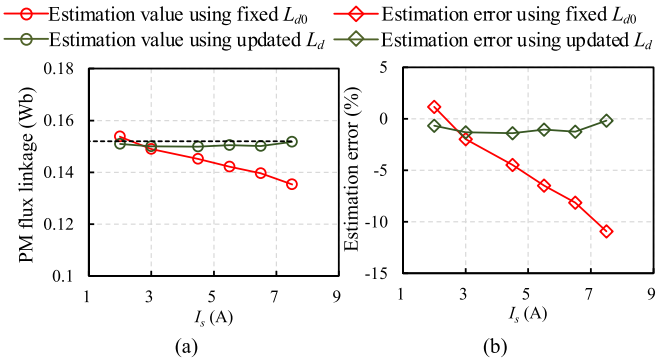

Fig. 12. Estimated PM flux linkages by using the fixed L_{d0} and online updated L_d at different load conditions under MTPA control, at MS2, 900 r/min. (a) Estimation value. (b) Estimation error.

Figs. 11 and 12 demonstrate the PM flux linkage estimation results against the current vector I_s under MTPA control at MS1 (0.263 Wb, 600 r/min) and MS2 (0.152 Wb, 900 r/min), in which the red and the green lines represent the estimation results when using the fixed d-axis inductance value (L_{d0}) and the online updated L_d, respectively. It can be easily observed that the estimation error under the fixed d-axis inductance increases gradually with the increase of load current at both MS1 and MS2. The maximum relative estimation errors are 8.6% at MS1, and 10.7% at MS2. While the maximum relative estimation errors are within 1.5% at both MS1 and MS2 when using the online updated d-axis inductance. It indicates that the PM flux linkage can be precisely estimated at different MSs under the MTPA control by using the proposed estimation method.

Figs. 13 and 14 present the PM flux linkage estimation results against d-axis current i_d under the FW control at MS1 (0.263 Wb, 1000 r/min) and MS2 (0.152 Wb, 1600 r/min). The q-axis current i_q is constant 3 A and the machine is not saturated in these experiments, namely the PM flux linkage will not be reduced when the load current is added. It can be easily seen that the estimation errors under the fixed d-axis inductance increase gradually with the increase of negative d-axis current at both MS1 and MS2. The maximum relative estimation errors are 16.3% at MS1 and 21.1% at MS2 respectively, which are larger than the errors under the MTPA control. While the maximum

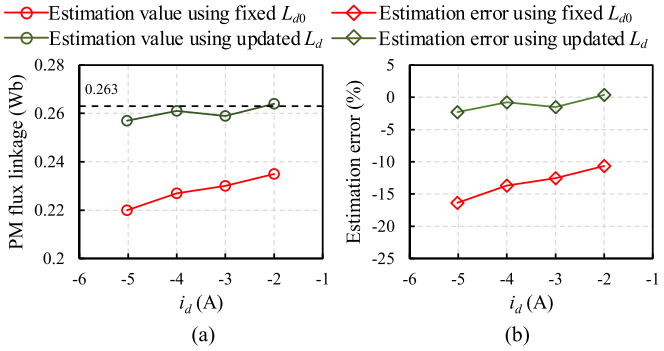

Fig. 13. Estimated PM flux linkages by using the fixed L_{d0} and online updated L_d at different load conditions under FW control, at MS1, 1000 r/min. (a) Estimation value. (b) Estimation error.

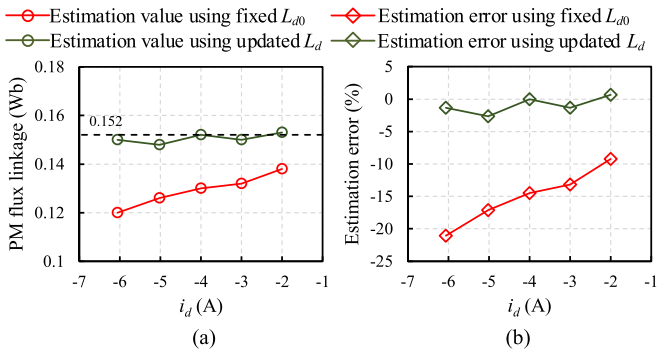

Fig. 14. Estimated PM flux linkages by using the fixed L_{d0} and online updated L_d at different load conditions under FW control, at MS2, 1600 r/min. (a) Estimation value. (b) Estimation error.

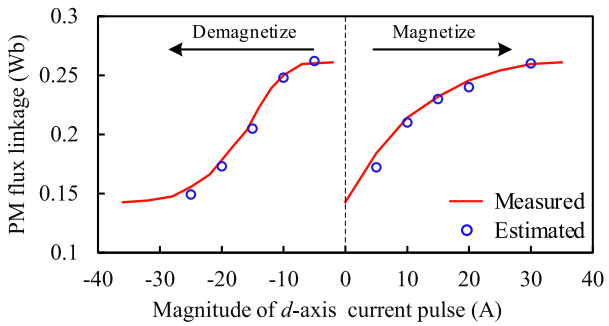

Fig. 15. Comparison of the measured and estimated PM flux linkages when applying different d-axis current pulses.

relative estimation errors are within 2.6% at both MS1 and MS2 when using the online updated d-axis inductance. It indicates that the PM flux linkage can be precisely estimated at different MSs under the FW control by using the proposed estimation method.

Fig. 15 shows a comparison of the measured and estimated PM flux linkages when applying various d-axis current pulses. It can be found that the PM flux linkages can be estimated within an acceptable error compared with the reference values whether in magnetization or demagnetization.

Figs. 16 and 17 show the PM flux linkage estimation results against the current vector I_s at MS1 (0.258 Wb, 600 r/min)

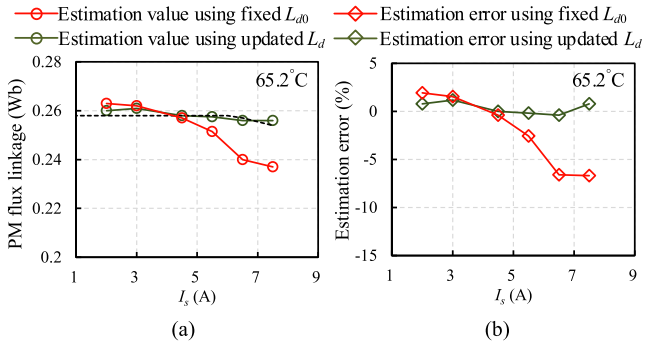

Fig. 16. Estimated PM flux linkages by using the fixed L_{d0} and online updated L_d at 65.2 °C and different load conditions under MTPA control, at MS1, 600 r/min. (a) Estimation value. (b) Estimation error.

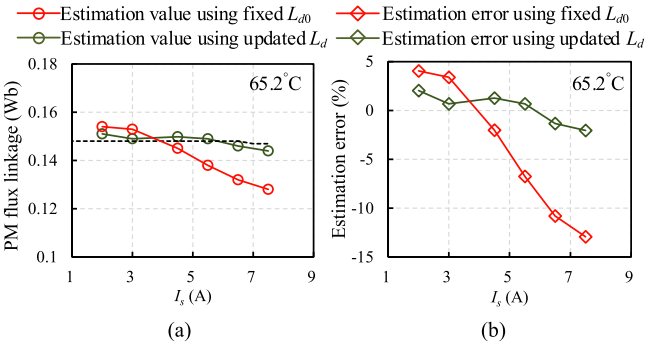

Fig. 17. Estimated PM flux linkages by using the fixed L_{d0} and online updated L_d at 65.2 °C and different load conditions under MTPA control, at MS2, 900 r/min. (a) Estimation value. (b) Estimation error.

and MS2 (0.147 Wb, 900 r/min), at 65.2 °C under the MTPA control. It can be clearly observed that the maximum relative estimation errors under the fixed d-axis inductance are 6.69% at MS1 and 12.9% at MS2, respectively. While the maximum relative estimation errors are within 2.0% at both MS1 and MS2 when using the online updated d-axis inductance. It indicates that the PM flux linkage can be precisely estimated at different MS and temperature conditions by using the proposed estimation method.

It should be noted that the actual PM flux linkages represented by the black dotted lines in Figs. 10–14, 16, and 17, which are achieved by analyzing the no-load back EMF and output torque, have a slight reduction at load condition, particularly at MS1, namely the saturation effect is considered.

C. Experimental Results of the Proposed Control Strategy

Fig. 18 shows the three MTPA trajectories, which are measured by experiments, calculated by using the fixed and estimated machine parameters, respectively. It can be clearly observed that the calculated MTPA trajectory by using the updated machine parameters is more consistent with the experimental trajectory at both MS1 and MS2, compared with the calculated trajectory by using the fixed machine parameters. It indicates that online parameter estimation is necessary for the calculation of MTPA trajectory, particularly at heavy load condition. Consequently, the optimal MTPA trajectories can be achieved to

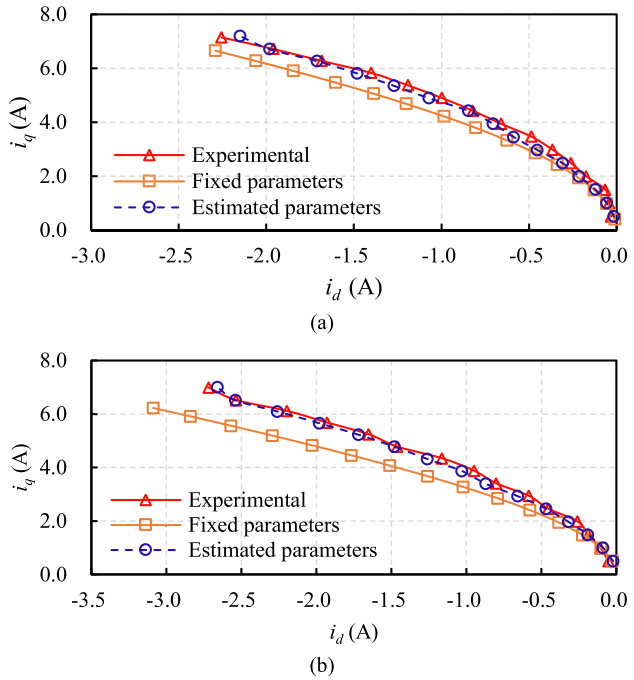

Fig. 18. Experimental MTPA trajectory and MTPA trajectories calculated by using fixed machine parameters and estimated parameters, respectively. (a) At MS1. (b) At MS2.

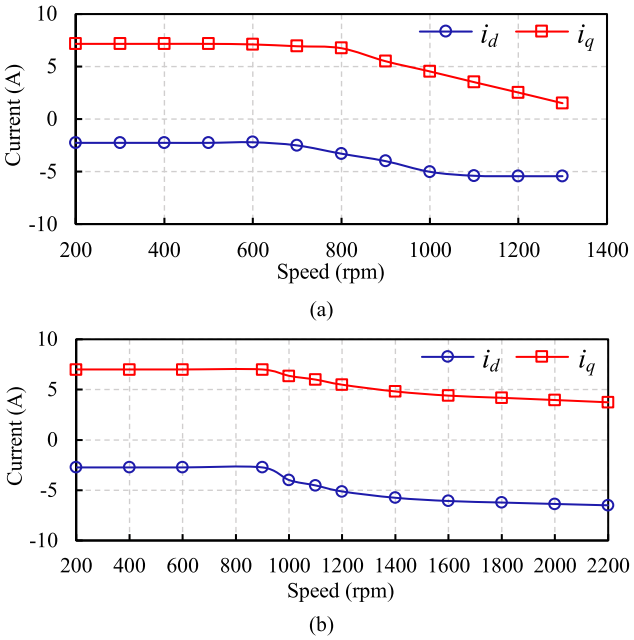

Fig. 19. Measured d-axis and q-axis currents versus speed curves by using the proposed strategy. (a) At MS1. (b) At MS2.

reduce the copper loss in the constant torque region, improving the machine efficiency.

Fig. 19 shows the dq-axis currents versus speed at MS1 and MS2, respectively. The maximum torques are produced by utilizing the reluctance torque through applying a continuous d-axis current. The on-load demagnetization can be avoided by restricting the magnitude of the d-axis current.

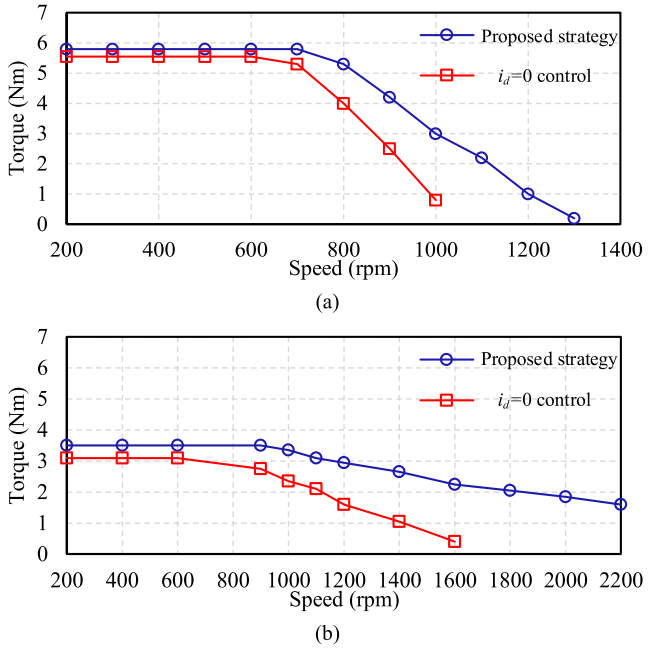

Fig. 20. Measured torque versus speed curves by adopting the proposed strategy and $i_d = 0$ control. (a) At MS1. (b) At MS2.

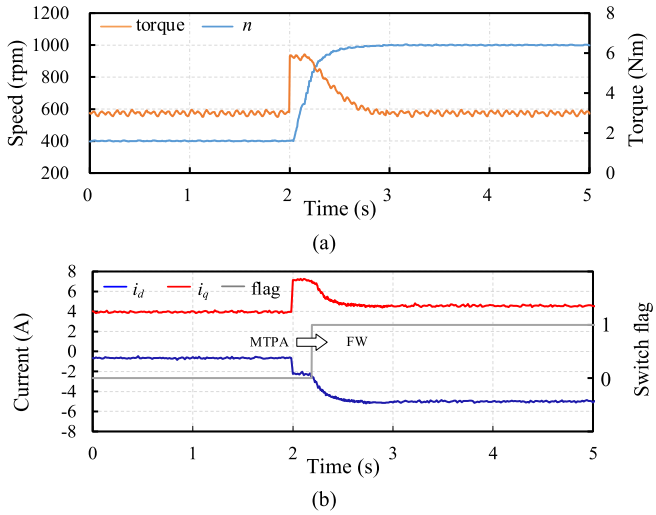

Fig. 21. Experimental dynamic responses of the machine with the proposed strategy when the speed increases from 400 to 1000 r/min with constant 3 N·m load, at MS1. (a) Waveforms of torque and speed. (b) Waveforms of dq-axis currents and switch flag between MTPA and FW.

Fig. 20 shows the curves of torque versus speed when using the proposed strategy and $i_d = 0$ control, at MS1 and MS2. It can be clearly observed that the output torque by using the proposed strategy is larger than the torque produced by $i_d = 0$ control in the constant torque region at each MS. More importantly, the speed ranges at both MS1 and MS2 are significantly extended in the constant power region.

Fig. 21 shows the dynamic responses of the machine with the proposed strategy when the speed increases from 400 to 1000 r/min with constant 3 N·m load, at MS1 (without MS change). In the proposed control strategy, the maximum torque under the

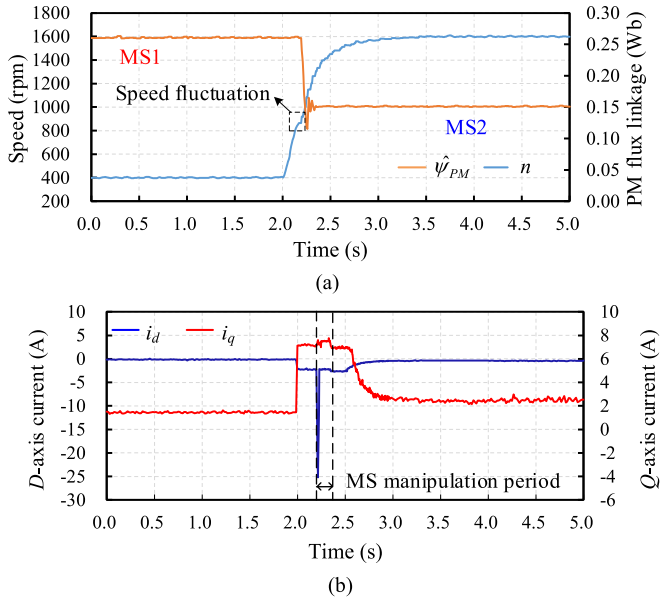

Fig. 22. Experimental dynamic responses of the machine with the proposed strategy when the speed increases from 400 to 1600 r/min with constant 1 N·m load, switching from MS1 to MS2. (a) Speed and estimated PM flux linkage. (b) *DQ*-axis currents.

MTPA control is immediately produced when the 1000 r/min speed command is given at 2 s. Then, the machine switches from MTPA to FW control with the increase of speed, as shown in Fig. 21. The optimal *dq*-axis currents are rapidly generated in the whole process so that the robustness and dynamic performance of the proposed control strategy are verified.

Fig. 22 presents the dynamic MS manipulation process with the proposed strategy when the speed increases from 400 to 1600 r/min, at 1 N·m load condition. The experimental waveforms of speed, PM flux linkage and *dq*-axis currents are simultaneously shown. When the machine speed is around 900 r/min, a -25 A i_d pulse is supplied into the stator winding and the machine is switched from MS1 to MS2. During the MS manipulation period, which is set as 150 ms in this article, the *q*-axis current is adaptively generated according to the speed controller to ensure the actual speed can track the reference speed well. While, in the other periods, the optimal *dq*-axis currents are generated by the proposed strategy to reduce the copper losses.

VI. Conclusion

This article proposes a novel control strategy combining the MTPA and FW controls for VFMM based on online parameter estimation. The major contributions of this article include the following.

1) The structured LADR-FFD current controller is able to greatly improve the current tracking performance.
2) The PM flux linkage can be precisely estimated by updating the online estimated *dq*-axis inductances at different MS, load, and temperature conditions.
3) The online-parameter-estimation-based MTPA control can obviously reduce the copper loss in the constant torque region at each MS.
4) The newly developed online-parameter-estimation-based FW control combining the feedforward and feedback approaches can further expand the speed range and improve the dynamic performance and stability of current regulation, in which the on-load demagnetization can also be avoided.

The effectiveness of the proposed control strategy has been verified by experiments.

References

[1] Z. Q. Zhu and D. Howe, "Electrical machines and drives for electric, hybrid, and fuel cell vehicles," *Proc. IEEE*, vol. 95, no. 4, pp. 746–765, Apr. 2007.
[2] H. Yang, S. Lyu, H. Lin, Z. Zhu, H. Zheng, and T. Wang, "A novel hybrid-magnetic-circuit variable flux memory machine," *IEEE Trans. Ind. Electron.*, vol. 67, no. 7, pp. 5258–5268, Jul. 2020.
[3] B. S. Gagas, K. Sasaki, T. Fukushige, A. Athavale, T. Kato, and R. D. Lorenz, "Analysis of magnetizing trajectories for variable flux PM synchronous machines considering voltage, high-speed capability, torque ripple, and time duration," *IEEE Trans. Ind. Appl.*, vol. 52, no. 5, pp. 4029–4038, Sep. 2016.
[4] T. Fukushige, N. Limsuwan, T. Kato, K. Akatsu, and R. D. Lorenz, "Efficiency contours and loss minimization over a driving cycle of a variable flux-intensifying machine," *IEEE Trans. Ind. Appl.*, vol. 51, no. 4, pp. 2984–2989, Jul. 2015.
[5] A. Athavale, D. J. Erato, and R. D. Lorenz, "Enabling driving cycle loss reduction in variable flux PMSMs via closed-loop magnetization state control," *IEEE Trans. Ind. Appl.*, vol. 54, no. 4, pp. 3350–3359, Jul. 2018.
[6] R. Antonello, M. Carraro, and M. Zigliotto, "Maximum-torque-per-ampere operation of anisotropic synchronous permanent-magnet motors based on extremum seeking control," *IEEE Trans. Ind. Electron.*, vol. 61, no. 9, pp. 5086–5093, Sep. 2014.
[7] S. Kim, Y. D. Yoon, S. K. Sul, and K. Ide, "Maximum torque per ampere (MTPA) control of an IPM machine based on signal injection considering inductance saturation," *IEEE Trans. Power Electron.*, vol. 28, no. 1, pp. 488–497, Jan. 2013.
[8] S. Y. Jung, J. Hong, and K. Nam, "Current minimizing torque control of the IPMSM using Ferrari's method," *IEEE Trans. Power Electron.*, vol. 28, no. 12, pp. 5603–5617, Dec. 2013.
[9] Y. A.-R. I. Mohamed and T. K. Lee, "Adaptive self-tuning MTPA vector controller for IPMSM drive system," *IEEE Trans. Energy Convers.*, vol. 21, no. 3, pp. 636–644, Sep. 2006.
[10] J. Chen, J. Li, and R. Qu, "Maximum-torque-per-ampere and magnetization-state control of a variable-flux permanent magnet machine," *IEEE Trans. Ind. Electron.*, vol. 65, no. 2, pp. 1158–1169, Feb. 2018.
[11] J. Chen, J. Li, R. Qu, and M. Ge, "Magnet-frozen-permeability FEA and DC-biased measurement for machine inductance: Application on a variable-flux PM machine," *IEEE Trans. Ind. Electron.*, vol. 65, no. 6, pp. 4599–4607, Jun. 2018.
[12] S. Bolognani, S. Calligaro, and R. Petrella, "Adaptive flux-weakening controller for interior permanent magnet synchronous motor drives," *IEEE J. Emerg. Sel. Topics Power Electron.*, vol. 2, no. 2, pp. 236–248, Jun. 2014.
[13] M. Tursini, E. Chiricozzi, and R. Petrella, "Feedforward flux-weakening control of surface-mounted permanent-magnet synchronous motors accounting for resistive voltage drop," *IEEE Trans. Ind. Electron.*, vol. 57, no. 1, pp. 440–448, Jan. 2010.
[14] Y. Kwon, S. Kim, and S. Sul, "Voltage feedback current control scheme for improved transient performance of permanent magnet synchronous machine drives," *IEEE Trans. Ind. Electron.*, vol. 59, no. 9, pp. 3373–3382, Sep. 2012.
[15] A. M. Aljehaimi and P. Pillay, "Operating envelopes of the variable-flux machine with positive reluctance torque," *IEEE Trans. Transport. Electrific.*, vol. 4, no. 3, pp. 707–719, Sep. 2018.
[16] P. Guglielmi, M. Pastorelli, and A. Vagati, "Cross-saturation effects in IPM motors and related impact on sensorless control," *IEEE Trans. Ind. Appl.*, vol. 42, no. 6, pp. 1516–1522, Nov./Dec. 2006.
[17] K. Liu and Z. Q. Zhu, "Online estimation of the rotor flux linkage and voltage-source inverter nonlinearity in permanent magnet synchronous machine drives," *IEEE Trans. Power Electron.*, vol. 29, no. 1, pp. 418–427, Jan. 2014.

[18] K. Liu, Z. Q. Zhu, Q. Zhang, and J. Zhang, "Influence of nonideal voltage measurement on parameter estimation in permanent-magnet synchronous machines," *IEEE Trans. Ind. Electron.*, vol. 59, no. 6, pp. 2438–2447, Jun. 2012.
[19] H.-W. Kim, M.-J. Youn, K.-Y. Cho, and H.-S. Kim, "Nonlinearity estimation and compensation of PWM VSI for PMSM under resistance and flux linkage uncertainty," *IEEE Trans. Control Syst. Technol.*, vol. 14, no. 4, pp. 589–601, Jul. 2006.
[20] T. Liu, Q. Li, Q. Tong, Q. Zhang, and K. Liu, "An adaptive strategy to compensate nonlinear effects of voltage source inverters based on artificial neural networks," *IEEE Access*, vol. 8, pp. 129992–130002, 2020.
[21] S. Morimoto, M. Sanada, and Y. Takeda, "Mechanical sensorless drives of IPMSM with online parameter identification," *IEEE Trans. Ind. Appl.*, vol. 42, no. 5, pp. 1241–1248, Sep./Oct. 2006.
[22] S. Kallio, J. Karttunen, P. Peltoniemi, P. Silventoinen, and O. Pyrhönen, "Online estimation of double-star IPM machine parameters using RLS algorithm," *IEEE Trans. Ind. Electron.*, vol. 61, no. 9, pp. 4519–4530, Sep. 2014.
[23] S. Cho, W. Shin, J. Park, and W. Kim, "A torque compensation control scheme of PMSM considering wide variation of permanent magnet temperature," *IEEE Trans. Magn.*, vol. 55, no. 2, Feb. 2019, Art. no. 8200105.
[24] M. N. Uddin and M. M. I. Chy, "Online parameter-estimation-based speed control of PM ac motor drive in flux-weakening region," *IEEE Trans. Ind. Appl.*, vol. 44, no. 5, pp. 1486–1494, Sep./Oct. 2008.
[25] C. Dai, T. Guo, J. Yang, and S. Li, "A disturbance observer-based current-constrained controller for speed regulation of PMSM systems subject to unmatched disturbances," *IEEE Trans. Ind. Electron.*, vol. 68, no. 1, pp. 767–775, Jan. 2021.
[26] L. Qu, W. Qiao, and L. Qu, "Active-disturbance-rejection-based sliding-mode current control for permanent-magnet synchronous machines," *IEEE Trans. Power Electron.*, vol. 36, no. 1, pp. 751–760, Jan. 2021.

Yuxiang Zhong received the B. Eng. degree from the Nanjing University of Astronautics and Aeronautics, Nanjing, China, in 2019. He is currently working toward the Ph.D. degree in electrical engineering with Southeast University, Nanjing, China.

His research interests include the control strategies of permanent magnet machines.

Heyun Lin (Senior Member, IEEE) received the B.S., M.S., and Ph.D. degrees in electrical engineering from the Nanjing University of Aeronautics and Astronautics, Nanjing, China, in 1985, 1989, and 1992, respectively.

From 1992 to 1994, he worked as a Postdoctoral Fellow with Southeast University, Nanjing, China. In 1994, he joined the School of Electrical Engineering, Southeast University, as an Associate Professor and became a Full Professor in 2000. His main research interests include the design, analysis, and control of permanent magnet motor, intelligent electrical apparatus, and electromagnetic field numerical analysis. He has authored more than 200 technical papers and the holder of 60 patents.

Dr. Lin is a Fellow of IET, a member of Electrical Motor and Apparatus Committee of Jiangsu Province, and Senior Member of both China Society of Electrical Engineering and China Electrotechnical Society.

Zhiyong Chen received the B. Eng. degree in electrical engineering and automation from Dalian Maritime University, Dalian, China, in 2019. He is currently working toward the M.Eng. degree in electrical engineering from Southeast University, Nanjing, China.

His research interests include the control strategies of permanent magnet machines and power electronics.

Shukang Lyu (Student Member, IEEE) received the B.Eng. degree in new energy science and engineering from Hohai University, Nanjing, China, in 2016. He is currently working toward the Ph.D. degree in electrical engineering with Southeast University, Nanjing, China.

His research interests include control strategies for permanent magnet machines and power electronics.

Hui Yang (Member, IEEE) received the B.Eng. degree from the Dalian University of Technology, Dalian, China, in 2011, and the Ph.D. degree from Southeast University, Nanjing, China, in 2016, respectively, all in electrical engineering.

From 2014 to 2015, he was supported by the China Scholarship Council through a one-year joint Ph.D. studentship with The University of Sheffield, Sheffield, U.K. Since 2016, he has been with Southeast University, where he has been an Associate Professor with the School of Electrical Engineering. From 2019 to 2020, he served as a Postdoctoral Fellow with the School of Electrical Engineering, The Hong Kong Polytechnic University. He has authored or coauthored more than 70 IEEE Transactions papers, and served as a peer reviewer of more than 10 IEEE journals. His research interests include novel permanent-magnet machines and drives with particular reference to variable-flux machines for electric vehicles and renewable energy applications.

Dr. Yang acts as an Editor for *World Electric Vehicle Journal*, a member of IEEE IES Electrical Machines Technical Committee, and IAS Electrical Machine Committee. He serves as a TPC-Track Chair of IEMDC 2021, as well as has served as Session Chair in Intermag 2018, IEMDC 2019, ICEMS 2019, and IEMDC 2021. He is invited as a tutorial speaker of PESA 2020 and IEMDC 2021. He was the recipient of Best Paper Awards in ICEMS 2014, EVER 2015, and ICEMS 2019, and the holder of 25 patents.